Estimating ocean heat transports and submarine melt rates in Sermilik Fjord, Greenland, using lowered acoustic Doppler current profiler (LADCP) velocity profiles

David A. SUTHERLAND,[1] Fiammetta STRANEO[2]

[1]*Department of Geological Sciences, University of Oregon, Eugene, OR, USA*
E-mail: dsuth@uoregon.edu
[2]*Department of Physical Oceanography, Woods Hole Oceanographic Institution (WHOI), Woods Hole, MA, USA*

ABSTRACT. Submarine melting at the ice–ocean interface is a significant term in the mass balance of marine-terminating outlet glaciers. However, obtaining direct measurements of the submarine melt rate, or the ocean heat transport towards the glacier that drives this melting, has been difficult due to the scarcity of observations, as well as the complexity of oceanic flows. Here we present a method that uses synoptic velocity and temperature profiles, but accounts for the dominant mode of velocity variability, to obtain representative heat transport estimates. We apply this method to the Sermilik Fjord–Helheim Glacier system in southeastern Greenland. Using lowered acoustic Doppler current profiler (LADCP) and hydrographic data collected in summer 2009, we find a mean heat transport towards the glacier of 29×10^9 W, implying a submarine melt rate at the glacier face of $650 \, \mathrm{m\,a^{-1}}$. The resulting adjusted velocity profile is indicative of a multilayer residual circulation, where the meltwater mixture flows out of the fjord at the surface and at the stratification maximum.

INTRODUCTION

Surface mass-balance studies have shown recently that the large ice sheets of Greenland and Antarctica are losing an increasing amount of mass, which ultimately ends up as fresh water, to the oceans (e.g. Rignot and others, 2011) and contributes to global sea-level rise. In Greenland, a significant fraction of the recent mass loss is attributed to the widespread acceleration, thinning and attrition of the glaciers over the past decade (Howat and others, 2007; Stearns and Hamilton, 2007) and several hypotheses have been proposed to explain it. Among these are rising air temperatures, which via increased surface melt can lead to increased lubrication at the bed and accelerated flow (Zwally and others, 2002) or can destabilize the floating tongue by feeding crevasses (Benn and others, 2007).

Alternatively, increasing basal runoff from surface melt (Motyka and others, 2011) and/or changes in the ocean circulation can lead to an increase in the heat transport at the glacier–ocean interface. An increased heat transport would have two potential impacts on the glacier. First, the increased heat content of the fjord waters would lead to a decrease in the ice melange typically located at the surface of the fjord in front of the glacier. This ice melange is thought to buttress the glacier, so any decrease in its volume or structural strength could lead directly to a surge in the glacier front (e.g. Amundson and others, 2010). Second, an increased heat transport in the subsurface waters of the fjord would lead to increased submarine melting at the glacier face. The increased melting could potentially drive two important feedbacks: (1) it would directly alter the shape and hence stability of the glacier front, potentially leading to calving events and acceleration of the glacier; and (2) it would drive an increase in the volume of upwelled water near the glacier front, which would drive an enhanced estuarine circulation in the fjord, leading to a more rapid flushing of fjord waters that potentially might result in additional heat transport (e.g. Motyka and others, 2011).

The difficulty in assessing these different hypotheses lies in the scarcity of observations inside Greenland's fjords, particularly the lack of any sustained direct measurements of velocity. Instead, previous studies have either inferred the circulation using hydrography and conservation of salt and volume, or used snapshots of velocity to calculate estimates of inflowing and outflowing waters. The latter method was used at Leconte Glacier, Alaska, to estimate the amount of heat available to melt the glacier face, but assumed an estuarine circulation scheme (Motyka and others, 2003), as did Rignot and others (2010) in their study on two small fjord systems in West Greenland. However, as shown by Mortensen and others (2011) and Straneo and others (2011), the circulation in Greenland's glacial fjords is dominated by strongly sheared currents that reverse on synoptic timescales of the order of days, which effectively mask the slower net circulation that transports heat to the glacier.

Here we remove the signal due to these modes by inferring their structure and amplitude and then subtract them from the velocity measured in the fjord. Explicitly, we use direct velocity observations from a major outlet fjord in southeastern Greenland, Sermilik Fjord (Fig. 1), to characterize the dominant modes of velocity variability and directly estimate heat transport to Helheim Glacier. We find evidence for the multilayer residual circulation cells of Straneo and others (2011) after accounting for the effects of the strongly varying intermediate circulation that is driven by changes at the fjord mouth (Klinck and others, 1981). Using these adjusted velocity profiles, we then calculate heat transport values driven by the residual circulation to infer submarine melt rates for Helheim Glacier.

PHYSICAL CHARACTERISTICS OF SERMILIK FJORD

Sermilik Fjord connects the continental shelf waters of the western Irminger Sea to Helheim Glacier, one of southeast Greenland's largest outlet glaciers (Fig. 1). The fjord runs

approximately north–south 16° east of north for ~70 km from its mouth to a junction with the subsidiary Helheim Fjord, which turns westward (287° along-fjord angle) for another ~20 km towards Helheim Glacier. Depths in the fjord shoal from ~900 m deep at the mouth to ~600 m deep at the entrance to Helheim Fjord, with a classic U-shaped structure in the across-fjord direction (Straneo and others, 2010). Hereafter, we refer to the Sermilik–Helheim Fjord system simply as Sermilik Fjord.

At the mouth of the fjord, several deep channels (depths >500 m) have been found, i.e. there is no evidence for a shallow sill in Sermilik Fjord, which impacts its dynamics significantly. Shelf waters in the Irminger Sea contain two main water masses: Atlantic water (AW), derived from the relatively warm and salty Irminger Current, and polar water (PW) that comes via the Arctic-origin East Greenland Current (EGC) and is relatively cold and fresh (Sutherland and Pickart, 2008; Straneo and others, 2010). These water masses are overlaid in the vertical, with PW typically occupying a 100–200 m upper layer on top of the denser AW layer (Fig. 2). This same basic stratification can be observed along Greenland's coast from Fram Strait, such as near Nioghalvfjerdsfjorden Glacier (Mayer and others, 2000), to West Greenland, such as near Jakobshavn Isbræ (Holland and others, 2008) or Godthabsfjord (Mortensen and others, 2011).

Previous studies of Kangerdlugssuaq Fjord (KG hereafter), located north of Sermilik Fjord in southeastern Greenland, have shed light on how shelf bathymetry might control the water masses found in these fjords. The waters in KG are influenced primarily via the EGC and its interaction with the Kangerdlugssuaq Trough (KG Trough). The KG Trough extends from the mouth of the fjord out to the shelf break at 600 m depth, creating a ~50 km wide deep conduit to the Irminger Sea. The KG Trough impacts the circulation of the EGC, with possible flow paths steered towards the Greenland coast under some conditions (Sutherland and Cenedese, 2009). The turning of the EGC towards KG brings some deeper Irminger Sea water up-canyon, potentially reaching the mouth of the fjord. Azetsu-Scott and Tan (1997) found waters up to 4°C in the KG Trough, evidence that Irminger Sea water is drawn towards the coast, and this observation was supported by more recent studies on the East Greenland Coastal Current (EGCC) (Sutherland and Pickart, 2008). However, waters inside the fjord were found to be cooler, evidence that either the warmest AW does not make it inside the fjord, or that intense mixing occurs along the transit across the shelf and through the KG Trough. Similar processes most likely bring AW to Sermilik Fjord, although the exact routing, timing and magnitudes are unknown.

SUMMER 2009 FIELD CAMPAIGN

From 19 to 24 August 2009 we collected hydrographic and velocity data from the M/V *Arctic Sunrise*, an ice-strength-ened vessel, at the stations indicated in Figure 1. We occupied a total of 42 stations, with the majority consisting of a conductivity–temperature–depth (CTD) cast along with a simultaneous lowered acoustic Doppler current profiler (LADCP) instrument. The CTD data came from a 6 Hz XR-620 RBR sensor that was calibrated pre- and post-deployment, while we used a 300 kHz RDI LADCP to obtain the velocity data. The velocity data were binned into 20 m depth bins after removing the ship motion and corrected for local
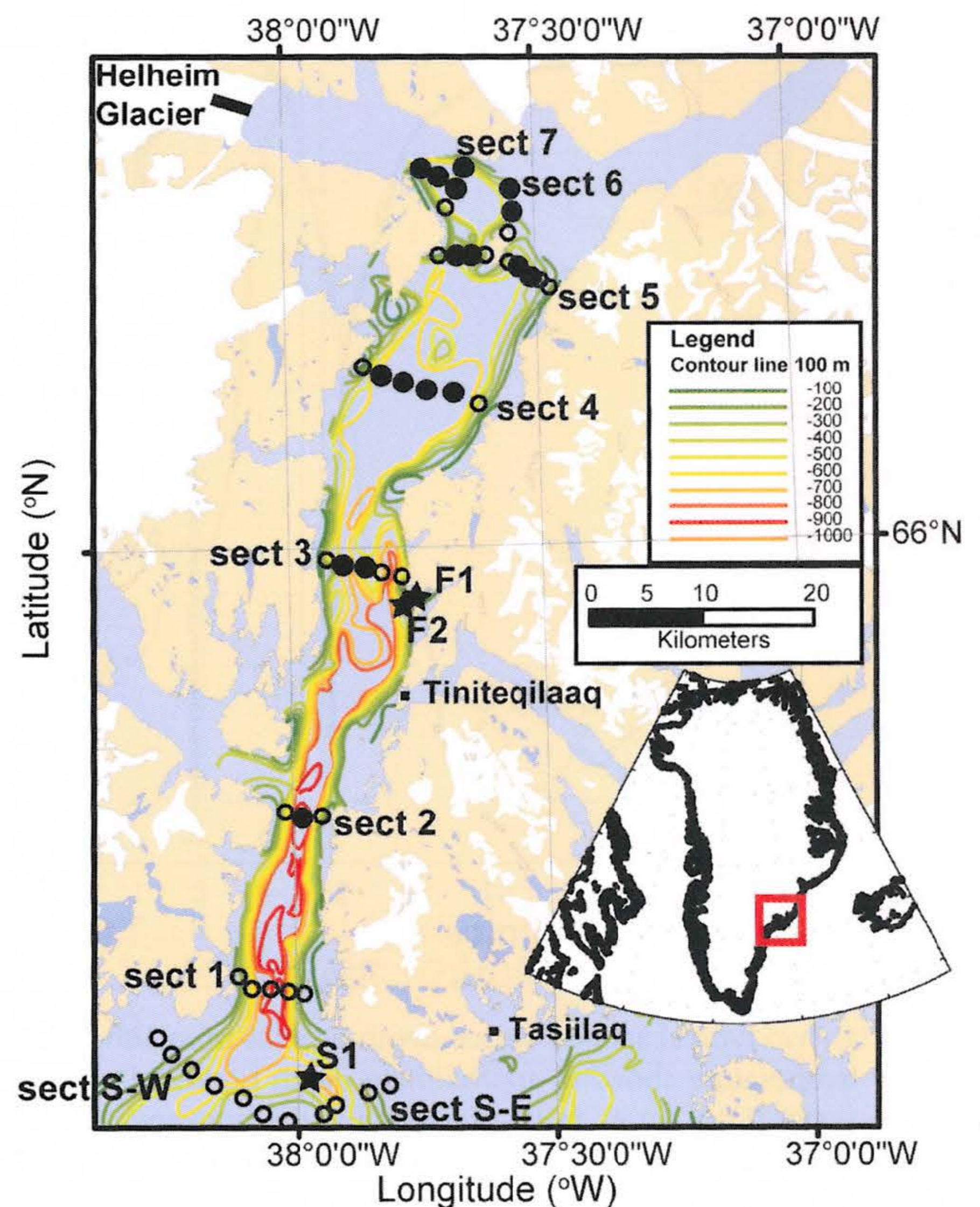

Fig. 1. Map of the study region, Sermilik Fjord, located in southeast Greenland (inset) overlaid on bathymetry contoured every 100 m (courtesy of F. Schjøt, 2010). Station locations (circles) are shown with their corresponding section name; filled circles indicate that the station was used in the LADCP analysis discussed in the text. Moorings (stars) are located in the fjord (F1, F2) and on the shelf (S1).

magnetic declination. A 12 kHz Knudsen echo sounder provided bathymetric data for this cruise. All temperatures reported here are potential temperatures.

The cruise preceded a barrier wind event along the southeast Greenland coast (Fig. 3a), which is characterized by strong downwelling favorable wind stress. Wind data came from the US National Centers for Environmental Prediction (NCEP) Reanalysis product provided by the Physical Sciences Division of the US National Oceanic and Atmospheric Administration/Office of Oceanic and Atmospheric Reseach/Earth and Space Research Laboratory (NOAA/OAR/ESRL), Boulder, Colorado) (http://www.esrl.noaa.gov/psd/; Kalnay and others, 1996), for a region outside the fjord mouth. Along-fjord wind stresses (winds parallel to coast at 216°) were small throughout the cruise period, although wind speeds on the shelf reached a maximum of 17 m s^{-1}, corresponding to a stress of 0.4 N m^{-2} (Fig. 3a). The LADCP casts were spaced from a few hours to 1 day apart, working from the head of the fjord towards the mouth (Fig. 3a). Tidal velocities estimated from the current-meter records (see below) were small inside the fjord, with magnitudes less than 0.015 m s^{-1}.

Time-series data come from two moorings in Sermilik Fjord near section 3 (F1 and F2; Fig. 1) during August 2009 and recovered in August 2010. Each mooring was designed to be low-profile to avoid icebergs and consisted of an anchor, a set of instruments and a subsurface buoy to keep the instrument upright. At the shelf site, the mooring S1
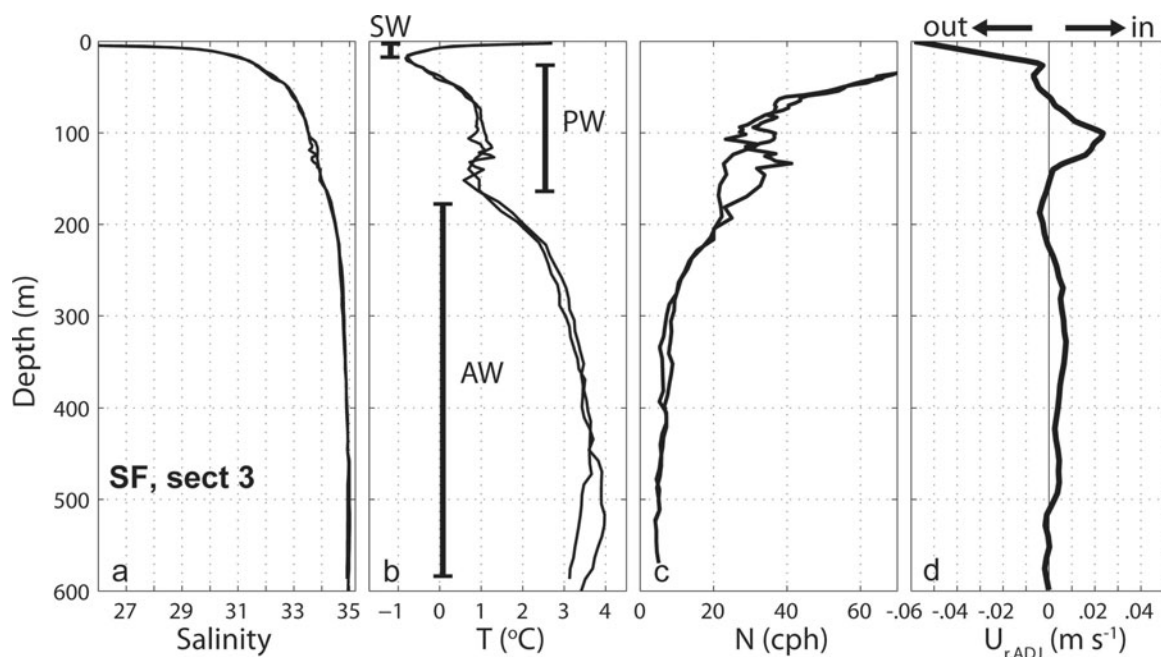
Fig. 2. (a) Two typical salinity versus depth profiles from Sermilik Fjord taken during summer 2009 at section 3 near mid-fjord. (b) As in (a) but for temperature showing approximate depth boundaries of the three main water masses: polar water (PW), Atlantic water (AW) and surface water (SW). (c) As in (a) but showing the buoyancy frequency N in cycles per hour. Note that N has been smoothed with a 10 m running average filter. (d) $U_{r,ADJ}$ profile transformed into depth space for Sermilik Fjord section 3, with arrows indicating in- or out-fjord flow.

consisted of a Nortek deep-water Aquadopp current meter that recorded velocity in hourly intervals at a mean depth of 298 m and a Seabird MicroCAT(+P) SBE37-SM instrument that measured salinity (S), temperature (T) and depth data in 15 min increments at a mean depth of 291 m. Inside the fjord, there was a shallow mooring that consisted of a Nortek deep-water Aquadopp current meter at 140 m and a Seabird MicroCAT(+P) SBE37-SM instrument that measured salinity, temperature and depth data in 15 min increments at a mean depth of 118 m. A second mooring recorded data at depth, with the current meter at 615 m and the MicroCAT at 601 m. The moored temperature and salinity data were checked with CTD casts taken during deployment and recovery for calibration. The mooring data will be used here primarily for context.

HYDROGRAPHIC OBSERVATIONS

The fjord hydrography observed in summer 2009 has been described elsewhere (Straneo and others, 2011). Here we focus on the general structure of the water masses in the vertical. Figure 2 shows typical profiles of S, T and stratification N, calculated from the buoyancy frequency

$$N^2 = (-g/\rho_0)\partial\rho/\partial z.$$

The summertime T–S structure midway up Sermilik Fjord shows the three main water masses present. Warm ($T \sim 3$–$4°C$) and salty ($S \sim 35$) AW occupies the deep layer, stretching from the subsurface stratification maximum at 150 m to the bottom (Fig. 2). Above the interface lies the colder ($T \leq 1°C$) and fresher ($S \sim 32$–33) PW. In a thin $\sim$10 m thick layer above the PW, a fresh warm water mass shows the influence of seasonal sea ice and runoff with salinities reaching $S < 20$, as well as thermal heating. This thin upper layer creates a seasonal surface maximum in stratification and is referred to here as surface water (SW). These

measurements are consistent with the two-layer structure seen in studies of the EGCC on the southeast Greenland shelf, which flows inshore of the shelf-break EGC/Irminger Current system near Sermilik Fjord (Sutherland and Pickart, 2008).

VELOCITY OBSERVATIONS

The LADCP data show pronounced variability relative to the hydrography, with highly sheared flows that changed dramatically by reversing sign or vertical structure in the 6 days of sampling. Figure 4a illustrates this with example casts from sections 3–7 that were occupied over a span of 2 days (Fig. 3a), yet had significant changes in shear and vertical structure. The vertical integral of the along-fjord velocity changes sign over the span of the cruise (Fig. 3b). This variability has been noted previously (Straneo and others, 2011), so here we try to condense and characterize the LADCP observations in a systematic way.

First, we choose to analyze deep casts where the fjord depth h is >400 m in order to fully capture the entire water column. In practice this meant keeping those stations towards the middle of the fjord. Then we excluded the mouth section, which was heavily influenced by shelf processes and the onset of the barrier wind event, which can alter the coastal current structure on the shelf (Sutherland and Pickart, 2008). This results in 17 usable casts (Fig. 1).

At each of these locations, we normalized the depth by the observed stratification. This was done by finding the depth of the first stratification maximum below the surface layer in each cast, z_{maxN2}, then applying a depth transformation to a new normalized depth coordinate system, z', where $z' = 0$ at the surface, 0.5 at z_{maxN2} and 1 at h. Figure 4 shows examples of this depth transformation. The effect of this normalization is to make the AW and PW layers the same thickness at each station, since the depth of the interface between them varies in time and position
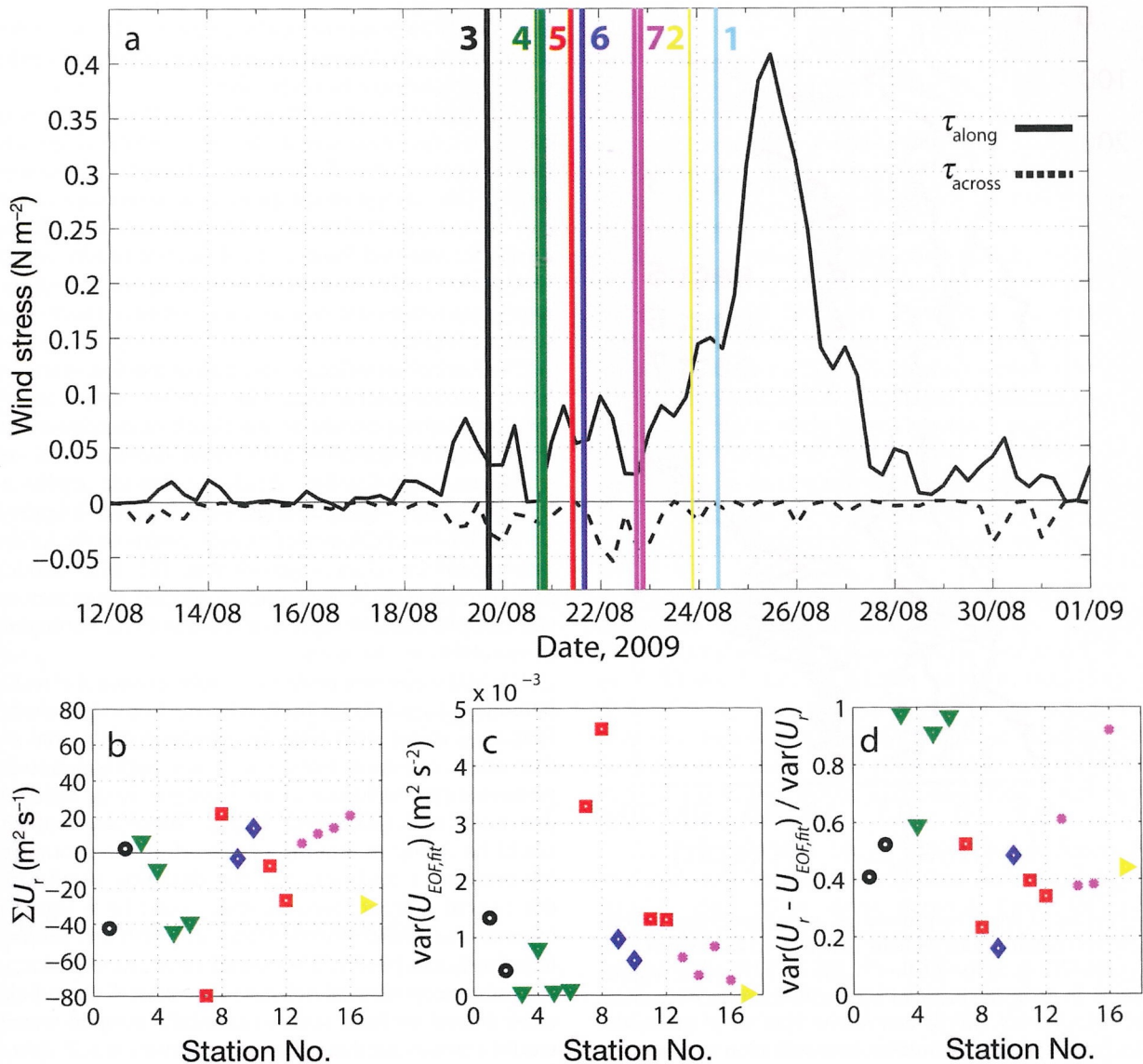
Fig. 3. (a) Along- and across-shelf wind stress during the cruise period in a region outside the fjord mouth, taken from the four times daily NCEP Reanalysis product (Kalnay and others, 1996). Downwelling favorable winds (216° to the southwest) have $\tau_{\text{along}} > 0$, while $\tau_{\text{across}} > 0$ is for winds towards the fjord. Dates are dd/mm. (b) ΣU_r, the vertical integral of the along-fjord velocity, U_r, for each station (colored by section as in (a)). (c) As in (b) but for var[$U_{\text{EOF,fit}}$], the variance of the mode 1 EOF fit to each station. (d) As in (b) but for the ratio of the residual variance, var[$U_{\text{EOF,fit}} - U_r$], to the original variance of U_r, var[U_r].

along-fjord. The SW is thin and essentially not recorded by the LADCP data, so we neglect its presence here.

Next, we rotated the LADCP velocities into along-fjord (U_r) and across-fjord (V_r) directions, using locally defined angles normal to each section, where $U_r > 0$ is flow into the fjord. The resulting set of normalized U_r profiles was averaged to give the mean U_r profile shown in Figure 5. The mean velocity profile is into the fjord and sheared over the upper water column, suggestive of flow out near the surface.

Analysis of the current-meter data (not shown) supports the LADCP observations and the time-series records of T and S presented by Straneo and others (2010), showing significant variability at seasonal, synoptic and higher frequencies most likely associated with high-mode internal waves. Velocities at the mid-fjord moorings fluctuated around zero at both depths, with a significant mean flow into the fjord at F1 (0.004 m s^{-1} at 44.5° into fjord). The mean flow at the deep current meter, F2, was not significantly different from zero.

MODES OF VELOCITY VARIABILITY

To assess the dominant vertical structure of the LADCP profiles, we use two independent analyses: empirical orthogonal function (EOF) analysis and normal-mode analysis. EOF analysis is a statistical technique which decomposes the variability into a set of modes that best describe the data but do not necessarily reflect any dynamical behavior (e.g. Emery and Thomson, 2004). By combining all the casts together from different locations, we are assuming that temporal variability dominates over horizontal position in the fjord, as each cast is now normalized in the vertical. This assumption is justified by examining the consistent hydrographic profiles taken along-fjord (Straneo and others, 2011) and moored temperature and salinity time series, which show coherent signals along the entire fjord that vary on timescales of days (Straneo and others, 2010).

The first three EOF modes of the normalized U_r profiles are shown in Figure 5. Modes 1–3 explain 52%, 30% and 8% of the variance, respectively. The structure of the first
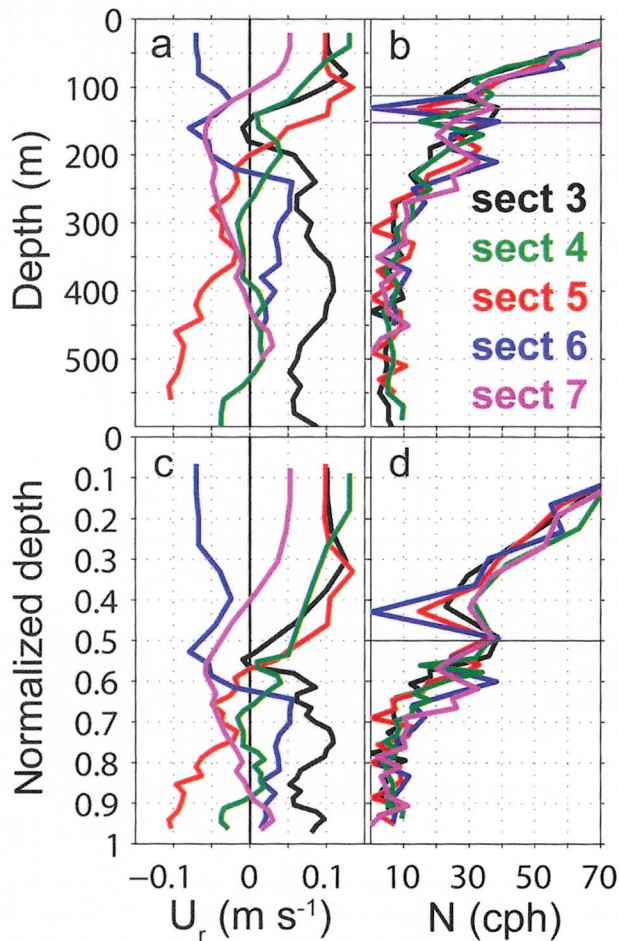
Fig. 4. Examples of depth transformation at representative stations located at the Sermilik Fjord sections indicated (colors match with timing shown in Fig. 3). (a) U_r (m s^{-1}) and (b) N (cph) in original depth space, showing the depth of maximum subsurface stratification (thin line). (c) U_r (m s^{-1}) and (d) N (cph) in z' space, the normalized depth, where the maximum stratification is at $z' = 0.5$.

EOF mode has one zero crossing near $z' = 0.5$ and resembles a first baroclinic mode, i.e. two-layer flow with velocities directed oppositely to each other.

We also calculate the vertical normal-mode structure based on the observed stratification profiles, transformed into z' space (for a discussion of normal modes, see Gill, 1982). The normal-mode analysis is physically based and can be compared directly to the EOF decomposition. The results for the first three vertical normal modes are shown in Figure 5 for a mid-fjord station at section 3. Similar modal structures are found using other stations taken in summer 2009.

The horizontal velocity structure of the first normal mode has a zero crossing near the interface depth at $z' = 0.5$ (Fig. 5c), corresponding to the depth of maximum vertical displacement (equivalent to the normalized vertical velocity structure shown; Fig. 5d). This vertical mode implies a two-layer flow with slightly stronger velocities in the upper layer.

The first two EOF modes closely resemble the calculated normal modes. This suggests that the EOF modes are showing physically meaningful modal structures in the velocity profiles that represent the dominant vertical modes of variability in the fjord.

Internal wave processes that could explain the first-mode baroclinic structure in the fjord arise from several sources. First, they might stem from the presence of internal seiches that are a common feature of other highly stratified and geometrically constrained fjord systems (e.g. Miles, 1974; Arneborg and Liljebladh, 2001). These internal seiches could be freely oscillating or forced at the mouth by the intermediate circulation, i.e. the changing stratification of the coastal current. Second, they could be a signal of an internal wave field inherited from the shelf and propagating into the fjord. Finally, they could be a combination of the low-frequency internal seiches, an internal wave field and other forced motions such as coastally trapped waves that would complicate the signal seen in the LADCP data.
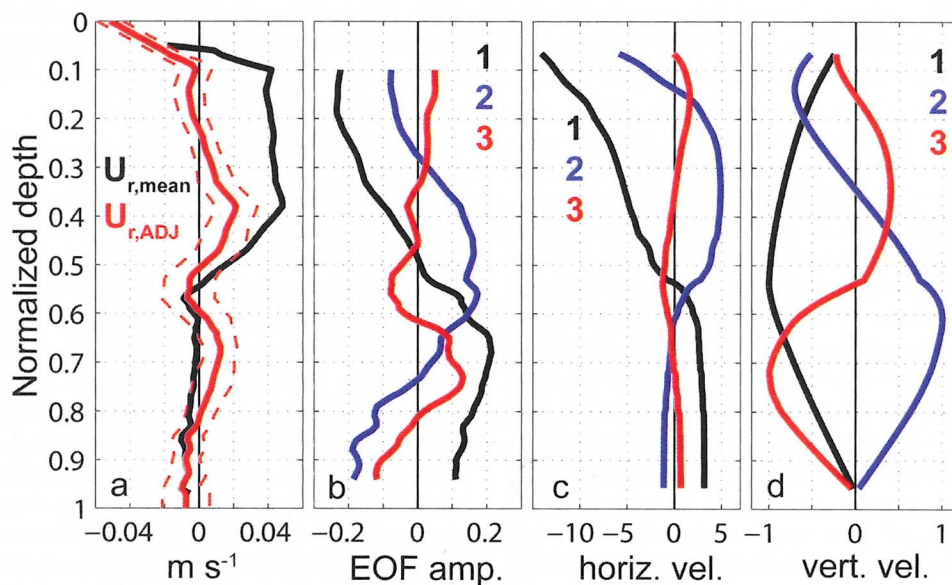

Fig. 5. (a) Mean of the along-fjord velocity from all the Sermilik LADCP casts, $U_{r,mean}$ (black line), and the adjusted along-fjord velocity profile, $U_{r,ADJ}$ (red line), with ± 1 standard error (dashed red lines). (b) Vertical structure of the first three EOF modes calculated from the set of LADCP casts. (c) Vertical structure of the horizontal velocity for the first three normal modes calculated from a summertime section 3 stratification profile. (d) As in (c) but for interface displacement (equivalent to vertical velocity).

For the purposes of this study, the precise mechanism does not matter explicitly, except that it exhibits a first-mode baroclinic structure that we try to remove. To identify the internal seiche process in the data would require more stations spatially and longer time series of casts at each station.

However, since internal seiches are commonly observed in lakes and other fjord systems (e.g. Arneborg and Liljebladh, 2001), we speculate that they might explain the variability observed in Sermilik Fjord. The internal seiche interpretation is supported by the fact that the EOF analysis was calculated using LADCP profiles located along the whole length of each fjord. This suggests the modal structures shown in the EOF analysis, and consistent with the normal-mode breakdown, have spatial coherence over the entire fjord, although more stations are needed to verify this claim.

One can calculate phase speeds based on the normal modes, which are physically akin to internal wave speeds, $c_n = (gH_{e,n})^{1/2}$, where $H_{e,n}$ is the equivalent depth of the nth mode (Gill, 1982). Then the natural periods of oscillation for mode 1 can be found assuming the internal seiche operates as a quarter-wave oscillator at the mouth, $T_n = 4L/c_n$, where T_n is the period and L is the length of the basin (Miles, 1974). Assuming $L \sim 70$ km for Sermilik Fjord and $c_1 = 1.1$ m s^{-1}, then $T_n = 71$ hours for the fundamental mode 1 structure. Other formulae exist for estimating internal seiche periods, such as Merian's formula (Miles, 1974), but previous studies have found these estimates to be accurate to within only ±20% so we do not report them here. Higher-mode seiches would have shorter periods as more waves would fit inside the basin.

MULTILAYER RESIDUAL CIRCULATION

Over a long time average, one might expect the mean velocity profile in the fjords to approach that of an estuarine circulation potentially divided into several stacked cells as argued by Straneo and others (2011), in that there must be a net outflow of water to balance the surface runoff and subglacial meltwater added. On shorter timescales, such as over the length of our fieldwork, we expect the circulation to be dominated by more highly sheared oscillatory flows forced by the intermediate circulation at the mouth, internal seiches and a strong internal wave field (Klinck and others, 1981; Straneo and others, 2010, 2011). Note that the magnitudes of the flows recorded by individual LADCP profiles (Fig. 4) are much larger than the mean flows in Sermilik Fjord recorded by the current meters over a year. Another complicating feature is the presence of stratification that might allow for multilayered residual flows to be set up. Evidence for these multiple cells was observed from hydrography in Sermilik Fjord (Straneo and others, 2011) and makes the use of a simple estuarine circulation scheme difficult and possibly invalid.

If we assume that the intermediate circulation variability and the dominant part of the internal wave field are mostly accounted for in the mode 1 EOF (Fig. 5b), then we can subtract out the mode 1 structure from each U_r profile. To do this, we fit the mode 1 EOF structure to each observed U_r profile separately and then take the mean of all the $U_r - U_{EOF,fit}$ profiles. Figure 3c shows the variance of the fit to the mode 1 EOF, $U_{EOF,fit}$, for each station. Along with Figure 3d, which shows the ratio of the residual variance to the original variance of U_r, var($U_r - U_{EOF,fit}$)/var(U_r), this gives an idea of how well the method either removes the mode 1 signal from

U_r or if a mode 1 signal is present at all. The residual variance is reduced by >40% at 13 of the 17 stations (Fig. 3d). The method performs well at each section except section 4, where three of the stations did not show a dominant baroclinic structure that could be removed.

Next we extend the shear in the upper part of the water column ($z' < 0.1$) to the surface and make the bottom boundary layer constant to the bottom ($z' = 1$). The first assumption is based on the notion that the thin SW waters will be flowing out-fjord and on visual observations during the 2009 fieldwork. Assuming a constant bottom layer velocity is the simplest assumption and is justified by the small variations in the deep water column. Interpolating the bottom velocity to zero has no significant effect on the results. In the surface layer, however, making a constant upper layer equal to the topmost measurement slightly decreased the heat transport magnitudes discussed below. Finally, we adjust the velocity profile so that there is no net transport, by subtracting a barotropic velocity of $u_{baro} = 0.014$ m s^{-1}.

The adjusted velocity profile $U_{r,ADJ}$ (Fig. 5a) has a maximum velocity of 0.06 m s^{-1} in the surface layer ($0 < z' < 0.1$), with a compensating inflow that has a mean of 0.01 m s^{-1} below, down to the interface depth ($0.1 < z' < 0.5$). Just below the level of maximum stratification (i.e. below the PW/AW interface) another layer of outflow is found with peak velocities of 0.01 m s^{-1} ($0.5 < z' < 0.6$) and another compensating inflow layer below ($0.6 < z' < 0.8$).

We interpret the $U_{r,ADJ}$ profile as evidence for the multiple cell residual circulation inferred from hydrographic data taken along Sermilik Fjord (Straneo and others, 2011). We hypothesize that the upper cell is driven by surface runoff, sea-ice melt and a portion of the subglacial meltwater discharged from the glacier face, while the lower cell is induced by the remaining portion of subglacial meltwater that does not penetrate past the PW/AW interface.

Transforming the $U_{r,ADJ}$ profile back into real depth space for a typical Sermilik Fjord station provides a striking illustration of these residual circulation cells. Figure 2d shows the $U_{r,ADJ}$ profiles for Sermilik section 3. In the surface outflow layer ($z < 20$ m), the waters have warmed and freshened considerably, most likely due to surface heating and the addition of fresh water (e.g. ice melt or runoff). Below this lies the relatively colder and fresh PW layer that is flowing into the fjord. Between the PW and AW layers near 150 m depth, the T and S structures are dominated by intrusions, with strong layering and evidence for mixing apparent in the profiles. This interleaving occurs at the top of the interface outflow, implying that shear-driven mixing is important to setting the T and S structure at this depth. The warmest and saltiest waters observed are in the lower inflow layer, corresponding to the AW coming into the fjord.

Thus it appears that the circulation in Sermilik Fjord, though heavily modulated by synoptic variability, does have an estuarine-like structure when one accounts for the dominant mode of variability. The presence of stratification and deep subglacial discharge complicate the estuarine flow, however, creating multiple residual circulation cells. Longer time series and more stations are necessary to test the realism of this circulation schematic.

We interpret the velocity profile as quasi-instantaneous, i.e. representative of those few days we sampled without the

Table 1. Heat transports, Q, based on $U_{r,\mathrm{ADJ}}$ and T data at sections in Sermilik Fjord (SF). Values given are means, with ranges in parentheses, calculated using various assumptions (see text). Inferred submarine melt rates Q_m are calculated from Q as described in the text. Ice melt rates M are based on a glacier area of $\sim 4.2\,\mathrm{km}^2$

Fjord (section)	Q $10^9\,\mathrm{W}$	Q_m $\mathrm{km}^3\,\mathrm{a}^{-1}$	M $\mathrm{m\,a}^{-1}$
SF-2	22 (11–28)	2.1 (1.0–2.7)	500 (250–630)
SF-3	27 (21–34)	2.6 (2.0–3.2)	610 (480–770)
SF-4	51 (39–64)	4.8 (3.7–6.1)	1100 (880–1400)
SF-5w	21 (15–26)	2.0 (1.4–2.5)	480 (340–590)
SF-7	24 (11–42)	2.2 (1.0–4.0)	540 (250–950)
Petermann*	310	29.5	26
Avangnardleq†	86 ± 14	8.2 ± 1.3	1400 ± 290
Kangilerngata†	6.3 ± 0.9	0.60 ± 0.09	950 ± 180
Eqip Sermia†	1.7 ± 0.3	0.16 ± 0.03	250 ± 70
LeConte‡	6.9 ± 2.8	0.40–0.65	2400–4500

*Johnson and others (2011). Stated ranges were ±50%. To calculate M, glacier area of 70 km long by 16 km wide was used. Petermann Glacier advances on average $\sim 1100\,\mathrm{m\,a}^{-1}$.
†Rignot and others (2010).
‡Motyka and others (2003). Stated range for Q was ±40% and given for Q_m and M.

noise of the intermediate circulation. However, it reflects the current state of freshwater input into the fjord due to surface runoff and subglacial discharge, which can be highly variable in time itself (Andersen and others, 2010).

HEAT TRANSPORT AND SUBMARINE MELT RATE

Using the $U_{r,\mathrm{ADJ}}$ velocity profiles and cross-fjord sections of temperature, we can estimate the heat transport inferred from this multilayered circulation. Since the heat transport calculation is sensitive to any net volume transport, we first construct velocity fields assuming the $U_{r,\mathrm{ADJ}}$ profile is constant across the fjord. Since the depth varies across each section, we adjust the velocity section with a new barotropic velocity to make the integrated transport equal to zero. At each section, we calculate the heat transport Q,

$$Q = C_p \rho_0 \iint U_{r,\mathrm{ADJ}}^* (T - T_f)\,\mathrm{d}x\,\mathrm{d}z$$

where C_p is the specific heat capacity of sea water $(3980\,\mathrm{J\,kg}^{-1}\,\mathrm{K}^{-1})$, ρ_0 is a reference density $(1027\,\mathrm{kg\,m}^{-3})$, T is temperature (K), T_f is the freezing point temperature that is a function of S and pressure, $U_{r,\mathrm{ADJ}}^*$ is the zero net transport velocity profile and the integrals are taken across fjord (x) and in the vertical (z). Changing the horizontal resolution of the cross-fjord depth profile ($\mathrm{d}x$) results in slightly different values of Q, which are reported below.

Table 1 shows the resulting heat transports at several sections along the fjord (Fig. 1). The heat transport is directed into the fjord towards the glacier with a mean of $29 \times 10^9\,\mathrm{W}$, ranging from 11 to $64 \times 10^9\,\mathrm{W}$. Note that instantaneous heat transports, calculated using the original $U_{r,\mathrm{mean}}$ profile before accounting for the intermediate circulation, have magnitudes 10–50 times greater as well as reversals in sign, i.e. $Q < 0$ (Straneo and others, 2011). The range for each section comes from calculating Q using different assumptions for extrapolating $U_{r,\mathrm{ADJ}}$ to the surface and bottom

(constant instead of extending the shear), by using different horizontal resolutions ($dx = 0.5$ and $1.0\,\mathrm{km}$) in the cross-fjord direction, as well as changing the interface depths to reflect the ambiguity in picking $z' = 0.5$ (e.g. Fig. 4).

To convert the heat transports into submarine melt rates, Q_m, at the glacier face, we estimate that 1 TW ($10^{12}\,\mathrm{W}$) will melt $\sim 95\,\mathrm{km}^3\,\mathrm{a}^{-1}$, assuming a latent heat of fusion of $334\,500\,\mathrm{J\,kg}^{-1}$, a density of ice of $930\,\mathrm{kg\,m}^{-3}$, an initial ice temperature of $-10^\circ\mathrm{C}$ and a specific heat of ice of $2100\,\mathrm{J\,kg}^{-1}\,\mathrm{K}^{-1}$. Corresponding melt rates for each section are listed in Table 1 and are not sensitive to the chosen parameter values. The mean Q_m for Sermilik Fjord is $2.7\,\mathrm{km}^3\,\mathrm{a}^{-1}$, with a range of 1.0–$6.1\,\mathrm{km}^3\,\mathrm{a}^{-1}$, based on the five sections listed.

Next, we estimate the melt rate for Helheim Glacier based on a glacier face area of $4.2\,\mathrm{km}^2$, assuming a glacier depth of 700 m and a width of 6 km. The resulting melt rates, M, are reported in $\mathrm{m\,a}^{-1}$ for comparison to other systems below. The mean M is $650\,\mathrm{m\,a}^{-1}$, with a range of 250–$1400\,\mathrm{m\,a}^{-1}$, again with the maximum at section 4, although the ranges over all the sections overlap.

To give a sense of the magnitude of these estimates, we can compare the melt rates with independent estimates of the freshwater input into Sermilik Fjord via surface runoff and subglacial discharge, as well as through calving ice. Mernild and others (2010) ran a hydrological model of the major glacier catchment areas surrounding Sermilik Fjord and found annual mean values of the combined surface runoff and precipitation of $Q_s = 6\,\mathrm{km}^3\,\mathrm{a}^{-1}$. Andersen and others (2010) argue that most of this surface runoff would emerge at depth along the glacier face, i.e. the majority of Q_s enters the fjord subglacially. Mernild and others (2010) calculated a separate subglacial runoff value of $Q_g = 0.5\,\mathrm{km}^3\,\mathrm{a}^{-1}$. Combined with Q_s, the total liquid freshwater discharge, Q_{FW}, into the fjord is $Q_{\mathrm{FW}} = 6.5\,\mathrm{km}^3\,\mathrm{a}^{-1}$. On the other hand, Andersen and others (2010) found $Q_g = 5.1\,\mathrm{km}^3\,\mathrm{a}^{-1}$ for the summer months of 2007–08 using a surface energy model validated with in situ observations. Thus, the melt-rate estimates from this study are approximately half the magnitude of the best estimates of Q_{FW}.

Compared to the solid freshwater flux, in the form of ice discharge due to calving at the glacier front, the submarine melt is small. Helheim Glacier produces about $27\,\mathrm{km}^3\,\mathrm{a}^{-1}$ of calved ice (Howat and others, 2007; Mernild and others, 2010). During the rapid-acceleration years 2004–06, Helheim peaked at $\sim 60\,\mathrm{km}^3\,\mathrm{a}^{-1}$ of ice discharge (Howat and others, 2007; Stearns and Hamilton, 2007).

The range of melt rates calculated here is similar to those found in West Greenland fjords listed in Table 1 (Rignot and others, 2010). Melt rates on ice shelves, such as Petermann Glacier or typical Antarctic systems, are usually much smaller (Johnson and others, 2011). In an Alaskan glacier system, Motyka and others (2003) found unusually high melt rates of 2400–$4000\,\mathrm{m\,a}^{-1}$, although these were most likely valid only over a short seasonal timescale. We reiterate a similar concern over the melt rates reported here: they should be thought of as quasi-instantaneous estimates of the submarine melt rates for the Sermilik Fjord–Helheim Glacier system. However, they represent a step forward in direct measurements of heat transport and corresponding melt rates from in situ observations. Previous studies did not account for the highly variable circulation found in these systems.

Though we attempted to account for the intermediate circulation by subtracting out the baroclinic flow observed

in Sermilik Fjord, the effects of the intermediate circulation play an important role in modulating heat transport. Internal seiches forced by the wind can generate internal waves, which drive vertical mixing and alter the ambient stratification of the fjord waters (e.g. Arneborg and Liljebladh, 2001). In addition, they have horizontal excursion length scales of tens of km, so they most likely alter the horizontal density gradient through mixing processes as well. This effect could feed back on the estuarine circulation that is driven primarily through buoyancy forcing and the along-fjord density gradient. Seasonal variability in the strength of the intermediate circulation, which is driven by seasonally varying winds, might impart a seasonal modulation to the heat transport values calculated above. In addition, surface runoff essentially shuts down in the winter (Straneo and others, 2011), so the multilayer residual circulation will look quite different during certain times of year. Future work should focus on extending the time period of these LADCP observations to see if the method holds over the entire year. Coupling these observations with full water column bottom-mounted ADCP records and temperature profiles would also help in reducing uncertainties in the heat transport calculations. In addition, the seasonality of the forcing suggests that a similar seasonality may exist in the fjord circulation and the resulting heat transport. Preliminary analysis of LADCP data in Kangerdlugssuaq Fjord supports this notion and will be presented in future work.

SUMMARY

Velocity data collected in summer 2009 support the notion that the circulation in Sermilik Fjord is complex, with the dominant structure akin to a first-mode baroclinic flow that changes on timescales of days. By accounting for this variability, heat transport estimates were made that were not contaminated by these strong flows. In Sermilik Fjord, the mean heat transport was 29×10^9 W, implying a submarine melt rate at Helheim Glacier of $650 \, \text{m a}^{-1}$.

The adjusted velocity profile implies a residual circulation that has two main pathways, with a surface outflow and a subsurface outflow, compensated by inflows in between. The subsurface outflow was located at the stratification maximum near the PW/AW interface that characterizes fjord waters in southeastern Greenland. The method should be applicable to other Greenland fjords with similar circulation characteristics, i.e. strong baroclinic flow, no sill and strong stratification.

ACKNOWLEDGEMENTS

REFERENCES

Amundson JM, Fahnestock M, Truffer M, Brown J, Lüthi MP and Motyka RJ (2010) Ice mélange dynamics and implications for terminus stability, Jakobshavn Isbræ, Greenland. *J. Geophys. Res.,* **115**(F1), F01005 (doi: 10.1029/2009JF001405)

Andersen ML and 14 others (2010) Spatial and temporal melt variability at Helheim Glacier, East Greenland, and its effect on ice dynamics. *J. Geophys. Res.,* **115**(F4), F04041 (doi: 10.1029/2010JF001760)

Arneborg L and Liljebladh B (2001) The internal seiches in Gullmar Fjord. Part I: dynamics. *J. Phys. Oceanogr.,* **31**(9), 2549–2566 (doi: 10.1175/1520-0485(2001)031<2549:TISIGF>2.0.CO;2)

Azetsu-Scott K and Tan FC (1997) Oxygen isotope studies from Iceland to an East Greenland Fjord: behaviour of glacial meltwater plume. *Mar. Chem.,* **56**(3–4), 239–251 (doi: 10.1016/S0304-4203(96)00078-3)

Benn DI, Hulton NRJ and Mottram RH (2007) 'Calving laws', 'sliding laws' and the stability of tidewater glaciers. *Ann. Glaciol.,* **46**, 123–130 (doi: 10.3189/172756407782871161)

Emery WJ and Thomson RE (2004) *Data analysis methods in physical oceanography*, 2nd edn. Elsevier, Amsterdam

Gill AE (1982) *Atmosphere–ocean dynamics*. Academic Press, San Diego, CA (International Geophysics Series 30)

Holland DM, Thomas RH, de Young B, Ribergaard MH and Lyberth B (2008) Acceleration of Jakobshavn Isbræ triggered by warm subsurface ocean waters. *Nature Geosci.,* **1**(10), 659–664 (doi: 10.1038/ngeo316)

Howat IM, Joughin IR and Scambos TA (2007) Rapid changes in ice discharge from Greenland outlet glaciers. *Science,* **315**(5818), 1559–1561

Johnson HL, Münchow A, Falkner KK and Melling H (2011) Ocean circulation and properties in Petermann Fjord, Greenland. *J. Geophys. Res.,* **116**(C1), C01003 (doi: 10.1029/2010JC006519)

Kalnay E and 21 others (1996) The NCEP/NCAR 40-year reanalysis project. *Bull. Am. Meteorol. Soc.,* **77**(3), 437–471

Klinck JM, O'Brien J and Svendsen H (1981) A simple model of fjord and coastal circulation interaction. *J. Phys. Oceanogr.,* **11**(12), 1612–1626 (doi: 10.1175/1520-0485(1981)011<1612:ASMOFA>2.0.CO;2)

Mayer C, Reeh N, Jung-Rothenhäusler F, Huybrechts P and Oerter H (2000) The subglacial cavity and implied dynamics under Nioghalvfjerdsfjorden glacier, NE Greenland. *Geophys. Res. Lett.,* **27**(15), 2289–2292 (doi: 10.1029/2000GL011514)

Mernild SH and 8 others (2010) Freshwater flux to Sermilik Fjord, SE Greenland. *Cryosphere,* **4**(4), 453–465 (doi: 10.5194/tc-4-453-2010)

Miles JW (1974) Harbor seiching. *Annu. Rev. Fluid Mech.,* **6**, 17–33

Mortensen J, Lennert K, Bendtsen J and Rysgaard S (2011) Heat sources for glacial melt in a sub-Arctic fjord (Godthåbsfjord) in contact with the Greenland Ice Sheet. *J. Geophys. Res.,* **116**(C1), C01013 (doi: 10.1029/2010JC00652)

Motyka RJ, Hunter L, Echelmeyer KA and Connor C (2003) Submarine melting at the terminus of a temperate tidewater glacier, LeConte Glacier, Alaska, USA. *Ann. Glaciol.,* **36**, 57–65 (doi: 10.3189/172756403781816374)

Motyka RJ, Truffer M, Fahnestock M, Mortensen J, Rysgaard S and Howat I (2011) Submarine melting of the 1985 Jakobshavn Isbræ floating tongue and the triggering of the current retreat. *J. Geophys. Res.,* **116**(F1), F01007 (doi: 10.1029/2009JF001632)

Rignot E, Koppes M and Velicogna I (2010) Rapid submarine melting of the calving faces of West Greenland glaciers. *Nature Geosci.,* **3**(3), 141–218 (doi: 10.1038/ngeo765)

Rignot E, Velicogna I, Van den Broeke MR, Monaghan A and Lenaerts J (2011) Acceleration of the contribution of the Greenland and Antarctic ice sheets to sea level rise. *Geophys. Res. Lett.,* **38**(5), L05503 (doi: 10.1029/2011GL046583)

Stearns LA and Hamilton GS (2007) Rapid volume loss from two East Greenland outlet glaciers quantified using repeat stereo satellite imagery. *Geophys. Res. Lett.,* **34**(5), L05503 (doi: 10.1029/2006GL028982)

Straneo F and 7 others (2010) Rapid circulation of warm subtropical waters in a major glacial fjord in East Greenland. *Nature Geosci.,* **3**(33), 182–186 (doi: 10.1038/ngeo764)

Straneo F and 6 others (2011) Impact of fjord dynamics and glacial runoff on the circulation near Helheim Glacier. *Nature Geosci.,* **4**(5), 322–327 (doi: 10.1038/ngeo1109)

Sutherland DA and Cenedese C (2009) Laboratory experiments on the interaction of a buoyant coastal current with a canyon: application to the East Greenland Current. *J. Phys. Oceanogr.,* **39**(5), 1258–1271 (doi: 10.1175/2008JPO4028.1)

Sutherland DA and Pickart RS (2008) The East Greenland Coastal Current: structure, variability and forcing. *Progr. Oceanogr.,* **78**(1), 58–77 (doi: 10.1016/j.pocean.2007.09.006)

Van den Broeke M and 8 others (2009) Partitioning recent Greenland mass loss. *Science,* **326**(5955), 984–986 (doi: 10.1126/science.1178176)

Zwally HJ, Abdalati W, Herring T, Larson K, Saba J and Steffen K (2002) Surface melt-induced acceleration of Greenland ice-sheet flow. *Science,* **297**(5579), 218–222 (doi: 10.1126/science.1072708)